Large-eddy-simulation-informed resolvent-based estimation of turbulent pipe flow

Filipe R. do Amaral [*]

Département Fluides, Thermique, Combustion, Institut Pprime-CNRS-Université de Poitiers-ENSMA, 86000 Poitiers, France

André V. G. Cavalieri[†]

Divisão de Engenharia Aeroespacial, Instituto Tecnológico de Aeronáutica, 12228-900 São José dos Campos, SP, Brazil

A resolvent-based methodology is employed to obtain spatiotemporal estimates of turbulent pipe flow from probe measurements of wall shear-stress fluctuations. Direct numerical simulations (DNSs) and large-eddy simulations (LESs) of turbulent pipe flow at a friction Reynolds number of 550 are used as databases. We consider a DNS database as the true spatiotemporal flow field, from which wall shear-stress fluctuations are extracted and considered as measurements. A resolvent-based estimator is built following our earlier work [Amaral *et al.*, J. Fluid Mech. **927**, A17 (2021)], requiring a model for the nonlinear (or forcing) terms of the Navier-Stokes equations system, which are obtained from another DNS database, as in our earlier work, and from a series of computationally cheaper LES databases with coarser grids; the underlying idea is that LESs may provide accurate statistics of nonlinear terms related to large-scale structures at a low computational cost. Comparisons between the DNS and the estimates indicate that sufficiently accurate results can be achieved with estimators built with statistics from LESs with an order of magnitude fewer grid points than the DNSs, with estimates closely matching the reference DNS results up to the buffer layer and reasonable agreement up to the beginning of the log layer.

I. INTRODUCTION

Estimation of space-time flow fluctuations from noisy, low-rank measurements is an interesting option for the understanding of turbulence physics, design of flow control strategies, and reconstruction of missing or corrupted data. For wall-bounded turbulent flows, wall quantities such as shear stress and/or pressure are usually employed as inputs for the estimation algorithms, as for practical applications the measurement of such quantities is easier to obtain than, e.g., the velocity components at a given distance from the wall. To build the estimator, model-based methodologies can be used [1–6], although it is also possible to conduct flow estimations based solely on data [7–10]. For both model- and data-driven methodologies, the basic idea is to obtain transfer functions between the measurements and the estimated flow state, bearing in mind that the model-based methodologies have the additional advantage of providing insight into the underpinning physics.

In recent years, the use of linear models to understand the physics that drive turbulent wall-bounded flows has become widespread. Linear models provide a simple framework to work with,

---

[*]filipe.ramos.do.amaral@univ-poitiers.fr

[†]andre@ita.br

and the emergence of tools such as resolvent analysis enables modeling coherent structures and self-sustaining mechanisms in flows [11–16]. In the resolvent framework, the Navier-Stokes system is written in state-space form, and the nonlinear terms are interpreted as external forcing terms [17–20], hence providing a convenient input-output formulation, relating the flow response and the forcing modes to nonlinear terms in the Navier-Stokes system.

The input-output formulation enables the use of control theory tools [21], which can be adapted to estimate the flow state components after low-rank measurements. Towne *et al.* [22] introduced a resolvent-based estimator for flow statistics, which was further generalized by Martini *et al.* [23] for time-domain estimates. For the latter case, in order to build the transfer functions between the low-rank measurements and the flow state components, it is necessary to inform the algorithm with the cross-spectral density (CSD) of the nonlinear terms of the Navier-Stokes system, treated as forcing. If the true forcing CSD is used, optimal estimates of time-varying flow quantities are obtained. Other forcing models provide sub-optimal estimates. Such estimates are not causal, as the full time series of sensor data is required for estimation; extension to causal estimation, using only past sensor information, is proposed by [24]. In our previous work, we have successfully applied the methodology developed by Martini *et al.* [23] to direct numerical simulation (DNS) of turbulent channel flow, using wall shear-stress and pressure low-rank measurements [25]. Results show a close agreement between estimates and reference DNS fluctuations in the near-wall region, and good agreement for large-scale structures throughout the channel. A key feature is the use of forcing statistics extracted from the DNS database, which leads to an optimal estimator but requires expensive simulation and postprocessing to obtain the forcing CSD. One option to model the forcing statistics is to consider it as spatially white noise. Amaral *et al.* [25] show that this is a good choice for near-wall structures estimates, close to where the measurements were taken, whereas far from the wall, the estimator failed to deliver good results. The work also explored the use of a standard eddy-viscosity model that Cess [26] and del Álamo and Jiménez [27] embedded within the linear operator to somehow account for the nonlinear terms that are missing in the linearized Navier-Stokes (LNS) system. The eddy viscosity improved the channel flow large-scale structure estimates but at the cost of worsening the near-wall structure estimates.

Chinta and Luhar [28] employed the resolvent framework to estimate the velocity field of turbulent channel flow after low-rank measurements. Their method differs from that of Martini *et al.* [23] as they compute the resolvent modes for various wave-number/frequency combinations and then assume that the flow state is a linear combination of such modes, calibrating linear coefficients after the input/measurements data. In other words, the method by Chinta and Luhar [28] seeks to identify the resolvent modes that best represent the measurement data. It is interesting to note that the inclusion of an eddy-viscosity model in the linear operator also had a dual effect in the results of Chinta and Luhar [28]: although it improved the flow statistics, it also increased the velocity field estimates errors.

Obtaining optimal resolvent-based estimators to turbulent flow was shown to be feasible in Ref. [25], but with a high computational cost related to the extraction of forcing statistics from a DNS database. In the present paper, we employ the Martini *et al.* [23] resolvent-based methodology to estimate the space-time velocity fluctuation components of turbulent pipe flow at friction Reynolds number $\mathrm{Re}_\tau \approx 550$ using wall shear-stress measurements. In addition to DNS, we also explore the capability of wall-resolved large-eddy simulations (LESs) to construct estimators. A first DNS database is used as the reference case from which we extract low-rank measurements of wall-shear stresses. A second DNS and the other LES databases provide the forcing (nonlinear) statistics to build the linear estimators. The underlying assumption is that the LES provides sufficiently accurate statistics of large-scale structures, including associated nonlinear terms, and thus may be used to construct estimators with near-optimal performance. Here we investigate the capability of such LES databases in the reconstruction of the space-time flow field, aiming to obtain a reliable and lower-cost estimator that could be used for various high-Reynolds-number flows of practical interest.

The remainder of the manuscript is organized as follows. Section II presents the methods employed in this work, including the resolvent-based estimator algorithm and details on the turbulent pipe flow simulations. Section III contains the results, including a direct comparison among the reference DNS and the estimators using the different strategies to model the nonlinear terms of the LNS equations, as well as metrics to evaluate the performance of each estimator. Finally, Sec. IV presents the conclusions of this study.

II. METHODOLOGY

A. Resolvent-based estimator

Let us begin by applying a Reynolds decomposition over the flow state, i.e., $q = \bar{q} + q'$, where $\bar{q}$ and q' denote mean flow and fluctuation around the mean flow components. In the resolvent framework, a forcing term is obtained gathering all nonlinear terms on q'. The vector of velocity components is given by $u = [u_x u_r u_\theta]$, with u_x, u_r, and u_θ as the streamwise, radial, and azimuthal velocity components, respectively. The full state vector is written as

$$q = [u\, p]^T, \tag{1}$$

with $q = q(x, r, \theta, t)$, where r and θ indicate the radial and azimuthal directions, respectively, t denotes time, and p is the pressure component.

The linear Navier-Stokes (LNS) equations in cylindrical coordinates can be written as

$$\partial_t u + u_r \partial_r \bar{U} e_x + \bar{U} \partial_x u = \nabla p + \frac{1}{\text{Re}} \nabla^2 u + f, \tag{2a}$$

$$\nabla \cdot u = 0, \tag{2b}$$

where ∂ denotes partial derivatives with respect to t, r, or x for time, radial, and streamwise directions, respectively, $\bar{U}$ is the mean turbulent velocity profile, ∇ is the gradient operator, Re is the Reynolds number based on bulk velocity, f denotes the forcing components, and e_x is the unit vector in the streamwise direction. For use in resolvent analysis, the forcing f includes the nonlinear terms in the Navier-Stokes equation, $f = (-u \cdot \nabla u)$, such that Eqs. (2b) are an exact rearrangement of the full Navier-Stokes system.

Regarding the forcing components, they are structured as

$$f = [f_x f_r f_\theta]^T, \tag{3}$$

with $f = f(x, r, \theta, t)$. Only molecular viscosity is considered in the present work, such that Eq. (2b) is exact if the full forcing f is used [29]. In the following, primes ($'$) will be dropped from the state and forcing notations for simplification.

In a discretized state-space form, considering a grid with N_r points in the radial direction, the LNS equations take the form

$$M \frac{dq(t)}{dt} = Aq(t) + Bf, \tag{4a}$$

$$z(t) = Cq(t) + n(t), \tag{4b}$$

where A denotes the linearized Navier-Stokes operator, B is the input matrix that restricts the forcing terms to appear only in the momentum equation, z is the system observation (measurements), C is the observation matrix that selects N_s sensor readings from the state vector (in the present paper, wall-shear stresses in the axial and azimuthal directions), and n is the measurement noise. M is a diagonal matrix whose entries are set to 1 and 0 for the momentum and continuity equations, respectively. The dependencies on wall-normal distance, y (or radial distance r), were dropped to simplify notations.

The state components can be written as a superposition of Fourier modes as

$$q(x, r, \theta) = \sum_m \sum_\alpha \int_{-\infty}^{\infty} \hat{q}(\alpha, r, m, \omega) e^{i(\alpha x + m\theta - \omega t)} d\omega, \tag{5}$$

where ω denotes frequency, α and m indicate longitudinal and azimuthal wave numbers, respectively, hats are used for Fourier-transformed quantities, m is constrained to be an integer number, and $i = \sqrt{-1}$. Similar to the azimuthal direction, a Fourier series is taken along x, since periodic boundary conditions are applied for the axial direction in the simulations considered here.

Equation (4b) can be written in the frequency domain as

$$\hat{z}(\omega) = [C(-i\omega M - A)^{-1} B]\hat{f}(\omega) + \hat{n}(\omega), \tag{6}$$

where dependencies on longitudinal (α) and azimuthal (m) wave numbers were also dropped to simplify notations.

The term $R = (-i\omega M - A)^{-1} = L^{-1}$ is the resolvent operator, which is well-posed once nonslip boundary conditions are enforced for the three velocity components. For pipe flow, the linear operator A is written in cylindrical coordinates [30], and linearization is around the mean turbulent profile, considered as known; the linearized operator becomes

$$A = \begin{bmatrix} -i\alpha\bar{U} + \frac{\Delta + r^{-2}}{\mathrm{Re}} & -D\bar{U} & Z & -i\alpha I \\ Z & -i\alpha\bar{U} + \frac{\Delta}{\mathrm{Re}} & -\frac{2imr^{-2}}{\mathrm{Re}} & -D \\ Z & \frac{2imr^{-2}}{\mathrm{Re}} & -i\alpha\bar{U} + \frac{\Delta}{\mathrm{Re}} & -imr^{-1} \\ i\alpha I & D + r^{-1} & imr^{-1} & Z \end{bmatrix}, \tag{7}$$

where $\Delta = -\alpha^2 I - (m^2 + 1)r^{-2} + r^{-1}D + D^2$, $D = \frac{d}{dr}$ is a diagonal matrix with the radial direction derivative operator (finite-differences scheme), I is the identity matrix, r and $\bar{U}$ are diagonal matrices containing the radial discretization and mean turbulent velocity profile, respectively, and Z is the zero matrix.

The actuation/input operator B is defined as

$$B = \begin{bmatrix} I & Z & Z \\ Z & I & Z \\ Z & Z & I \\ Z & Z & Z \end{bmatrix}, \tag{8}$$

whereas the observation/output operator C is given by

$$C = \begin{bmatrix} D_{\mathrm{wall}} & Z & Z & Z \\ Z & Z & D_{\mathrm{wall}} & Z \end{bmatrix}, \tag{9}$$

where D_{wall} means that only the derivatives corresponding to the pipe wall (i.e., the corresponding line of the differentiation matrix) are taken into account. The diagonal matrix M is written as

$$M = \begin{bmatrix} I & Z & Z & Z \\ Z & I & Z & Z \\ Z & Z & I & Z \\ Z & Z & Z & Z \end{bmatrix}. \tag{10}$$

From the definitions above, it is possible to obtain an optimal linear transfer function ($\hat{T}_q$) between the system observation ($\hat{z}$) and the estimated flow state components ($\hat{\tilde{q}}$), such that

$$\hat{\tilde{q}} = \hat{T}_q \hat{z}, \tag{11}$$

where $\hat{T}_q$ is the transfer function, and dependency on frequency ω was dropped to simplify notations. The tilde superscript denotes estimates.

Martini *et al.* [23] derived an expression for $\hat{T}_q$ that is based on the minimization of the error between the true ($\hat{f}$) and estimated ($\hat{\tilde{f}}$) forcing terms. The resulting transfer function is given by

$$\hat{T}_q = RBP_{ff}H^*(HP_{ff}H^* + P_{nn})^{-1}, \tag{12}$$

where $H = CRB$ is the resolvent operator including the observation (C) and actuation (B) matrices, and $P_{nn} = \langle \hat{n}\hat{n}^* \rangle$ and $P_{ff} = \langle \hat{f}\hat{f}^* \rangle$ are the CSDs of sensor noise and forcing, respectively. The asterisk (*) indicates a Hermitian transpose.

To build the transfer function, it is necessary to specify *a priori* the forcing CSD (P_{ff}). When true forcing statistics are known, Eq. (12) provides the optimal linear estimator, whereas other models for the forcing CSD provide suboptimal estimators. In the present paper, we focus on the modeling of P_{ff} through DNS and LES, extracting the nonlinear terms of the Navier-Stokes system direct from the simulations. Many other strategies can be employed to address the forcing statistics in the context of linear modeling for turbulent flows, such as, e.g., entropy-based modeling [31] or resolvent-based proper orthogonal decomposition (RESPOD) [32], among others. The reviews by Zare *et al.* [33] and Jovanović [34] explore the importance of the forcing statistics, and the means to obtain it, in the context of modeling and control of turbulent flows.

The measurement noise statistics (P_{nn}) must also be considered to evaluate the transfer function, and nonzero noise in the sensor readings can reduce the estimation efficiency [23]. In the cited work, it is shown that if the sensor readings are separated into a noiseless component and a noise component, the noiseless reading can only be recovered for small values of the measurement noise. Larger noise levels lead to smaller estimated components. In the present study, as the data are obtained directly from the simulations, the measurement noise is virtually nonexistent. Nevertheless, such a component regularizes the estimation, keeping the problem well-posed [23].

The transfer function obtained through Eq. (12) is noncausal, although it is possible to extend this approach to causal estimations through the Wiener-Hopf formalism, as addressed by Martini *et al.* [24] and Audiffred *et al.* [35]. As the focus of this work is on the applicability of using LES forcing statistics to build estimators, optimal causal transfer functions will be left for future work.

The snapshots are reconstructed in space and time according to the procedures briefly addressed below. First, it is necessary to take the inverse Fourier transform of the transfer function $\hat{T}_q$, Eq. (12), in order to return to time domain and obtain T_q,

$$T_q(\alpha, r, m, t) = \int_{-\infty}^{\infty} \hat{T}_q(\alpha, r, m, \omega)e^{i\omega t} d\omega. \tag{13}$$

Hence, the time-domain transfer function T_q must be convolved with the measurements/observations z to evaluate the state estimate in time domain $\tilde{q}$,

$$\tilde{q}(\alpha, r, m, t) = \int_{-\infty}^{\infty} T_q(\alpha, r, m, \tau)z(\alpha, r, m, t - \tau)d\tau. \tag{14}$$

Finally, double inverse Fourier transforms in the azimuthal and longitudinal directions are taken in order to return from the wave-number domain to physical space,

$$\tilde{q}(x, r, \theta, t) = \sum_m \sum_\alpha \tilde{q}(\alpha, r, m, t)e^{i\alpha x + im\theta}. \tag{15}$$

Note that although the notation $\tilde{q}$ is used on both sides of Eq. (15), on the left-hand side the estimated state is a function of the physical domain variables, i.e., (x, r, θ, t), whereas on the right-hand side, the state is a function of the wave-number domain variables, i.e., (α, r, m, t).

It is also possible to model the forcing statistics (P_{ff}), which provides a cheaper and suboptimal estimator. Another option is to consider an eddy-viscosity model in the linear operator A, Eq. (7), to somehow take into account the nonlinear terms of the Navier-Stokes system, as discussed by Symon *et al.* [36], Morra *et al.* [29], and Amaral *et al.* [25]. Appendix A addresses the linear operator
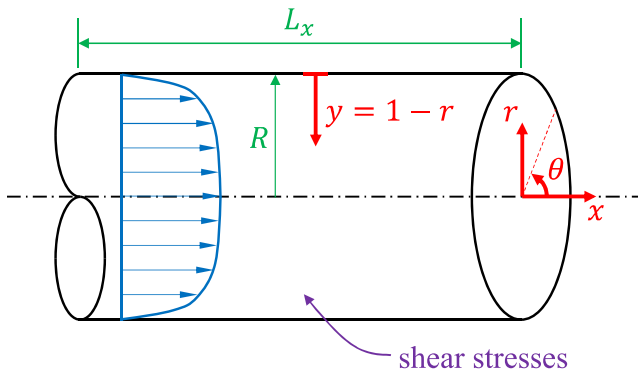
FIG. 1. Sketch of the channel flow geometry, dimensions (green), coordinate system (red), mean flow (blue), and wall measurements employed to perform the estimations (purple).

containing an eddy-viscosity model. In this case, the forcing statistics are considered as white noise in space. We will consider both cheap estimators to compare them with the LES ones.

B. Numerical simulations

To generate the databases, we conducted numerical simulations with the OPENPIPEFLOW code [37]. Periodic boundary conditions were assumed in the streamwise and azimuthal directions. Figure 1 shows a sketch of the geometry and coordinate system employed in this study.

For all simulations, the pipe length is $L_x = 10R$, where R is the pipe radius and the bulk Reynolds number is $\mathrm{Re}_b = \frac{U_b D}{\nu} = 19\,000$, where U_b is the bulk velocity, $D = 2R$ is the pipe diameter, and ν is the kinematic viscosity. Table I shows the parameters for all cases, including the number of radial (N_r), streamwise (N_x), and azimuthal (N_θ) grid points, the mesh discretization in the streamwise (Δx^+), azimuthal [$(R\Delta\theta)^+$], and radial (Δr^+) directions, and the mesh points ratio with respect to the DNS case (N/N_{DNS}). Plus symbols denote inner (wall and/or viscous) units. The data extracted from the simulations to obtain the measurements, forcing components, and comparisons with the reference DNS components contain 5000 snapshots, and the time step based on outer units is $\Delta t = 0.1$. Cases starting with D denote DNS, whereas the letter L indicate LES, carried out using the Smagorinsky [38] subgrid scale model, with a Smagorinsky constant set as $C_s = 0.05$; the wall damping function of van Driest [39] was used. As estimations lose accuracy for large wave numbers, only the lowest 16 and 32 streamwise and azimuthal wave numbers were used to construct the estimators. Welch's method [40] was employed to evaluate the forcing and state components statistics, with blocks containing $N_{fft} = 512$ time steps and 75% overlap. Appendix B shows the

TABLE I. Numerical simulation parameters.

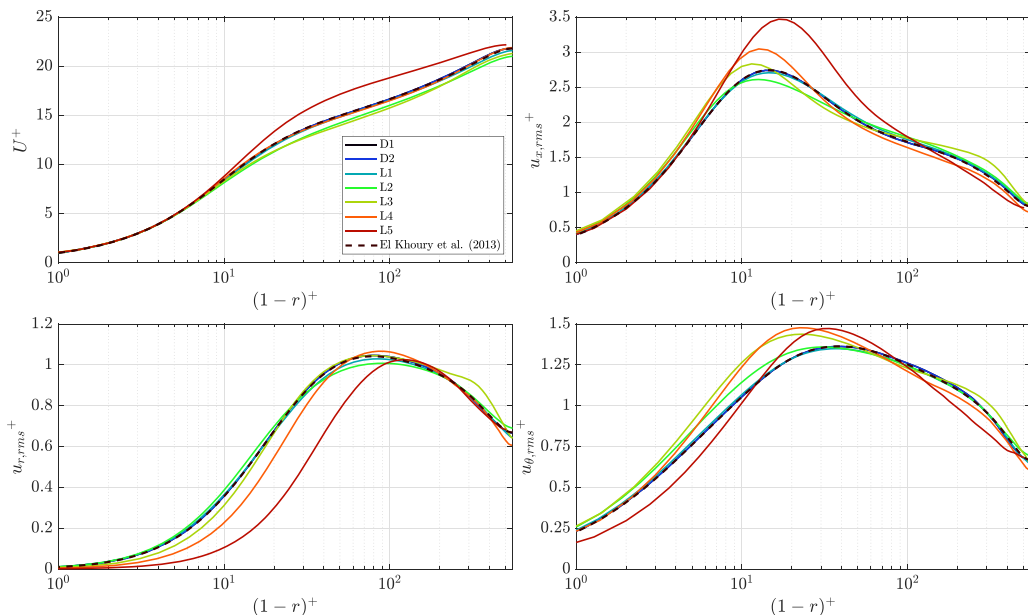| Case	Re_τ	N_r	N_x	N_θ	Δx^+	$(R\Delta\theta)^+$	Δr^+	N/N_{DNS}
D1	550.3	128	528	528	10.4	6.5	0.07–6.3	1.000
D2	550.3	128	528	528	10.4	6.5	0.07–6.3	1.000
L1	554.1	96	288	288	18.9	11.9	0.4–14.7	0.223
L2	568.6	96	192	192	28.6	18.0	0.4–15.2	0.099
L3	569.1	64	96	96	59.3	37.2	0.7–22.2	0.017
L4	551.8	64	64	64	86.1	54.1	0.7–22.9	0.007
L5	509.6	64	32	32	159.3	100.1	0.7–22.9	0.002

FIG. 2. Validation of the numerical simulations with reference DNS results from El Khoury *et al.* [41]: mean flow velocity profile (top-left frame), axial (top-right frame), radial (bottom-left frame), and azimuthal (bottom-right frame) velocity profiles.

results of the block size convergence test, justifying the use of $N_{fft} = 512$. A Hann window was applied to each block to minimize spectral leakage.

The simulations were validated with reference DNS results by El Khoury *et al.* [41], as shown in Fig. 2. Cases D1, D2, and L1 show close agreement with the reference simulations, regarding mean flow profile, axial, azimuthal, and radial velocity fluctuations, almost perfectly matching the results by El Khoury *et al.* [41]. The coarser grid cases (L2, L3, L4, and L5) progressively deteriorate the agreement, with the L5 case showing strong mismatch with all quantities, as expected for coarser LES.

Due to computational cost and storage limit issues, the same downsampling strategy adopted in Amaral *et al.* [25] was followed here, with only the first N_α streamwise and N_m azimuthal wave numbers retained to perform the estimates, according to the values shown in Table II. Hence, the databases were compressed by a ratio of $N_x N_\theta / (N_\alpha N_m)$. The filtered fields nonetheless retain the bulk of turbulent fluctuations, i.e., the peaks of the spectra in the wave-number domain are still present after the filtering procedure. Figure 3 shows the variances for the unfiltered and filtered D2

TABLE II. Wave-number cutoff parameters used to downsample the simulations.

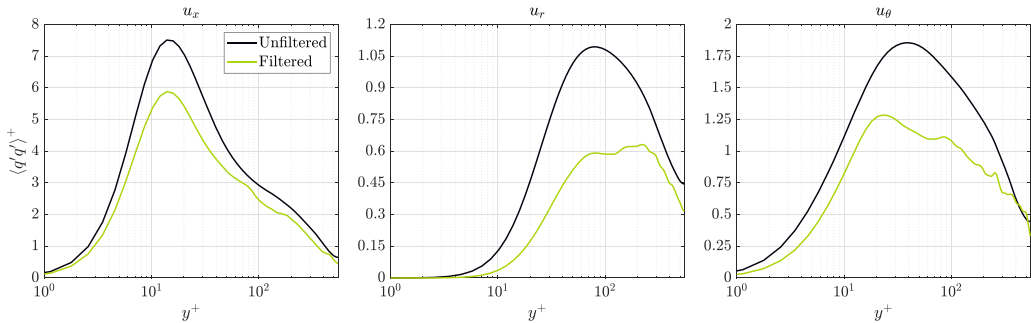| Case	N_α	N_m	α_{cut}	m_{cut}	$R\lambda_\theta{}^+_{\text{cut}}$	$\lambda_m{}^+_{\text{cut}}$	Downsampling ratio
D1	32	48	9.425	47	365.873	73.368	182
D2	32	48	9.425	47	365.873	73.368	182
L1	32	48	9.425	47	365.873	73.368	54
L2	32	48	9.425	47	365.873	73.368	24
L3	32	48	9.425	47	365.873	73.368	14
L4	24	12	6.912	12	498.918	313.480	6
L5	24	12	6.912	12	498.918	313.480	3

FIG. 3. Comparison between the variances of the unfiltered and filtered D2 database. Frames, from left to right: streamwise, radial, and azimuthal velocity components.

database and the streamwise, radial, and azimuthal velocity components, indicating that at least half of the variance of each component is retained by the filtering. The other DNS and LES databases follow similar trends. Table II also displays the employed cutoff values in terms of streamwise and azimuthal wave numbers in outer units, α_{cut} and m_{cut}, respectively, the streamwise and azimuthal wavelengths in inner/wall units, $\lambda_x^+{}_{cut}$ and $R\lambda_\theta^+{}_{cut}$, respectively, and the downsampling ratios.

Wall shear-stress measurements in the axial and azimuthal directions were extracted from the D1 database. The other databases, i.e., D2, L1, L2, L3, L4, and L5, were employed to construct the estimator transfer functions by extracting the forcing statistics P_{ff} and the mean velocity profile. We thus avoided, even for the DNS-based estimator, the use of the *ground-truth* data from the D1 simulation; a separate DNS was conducted, with different initial conditions but similar statistics, to ensure that the estimator has no knowledge of the ground-truth data other than the wall measurements. It is thus important to remark that the estimators employed in this study have no information from the D1 case. The LES databases, which have coarser grids, significantly reduce the computational cost, due to the lower number of grid points, but in turn lead to suboptimal estimators. In this work, we employ P_{ff} obtained in simulations that may have different grids from the measurements database D1 (see Table I). Hence, after the evaluation of the transfer functions $\hat{T}_q$, they are interpolated to a grid equivalent to that of the measurements database D1. Moreover, when the database employed to extract the forcing statistics does not contain data for a given pair (α, m), the forcing terms are modeled as white noise in space. The noise CSD (P_{nn}) was defined as machine precision, as we deal with DNS data mimicking measurements.

III. RESULTS

A. Snapshot estimates

Figures 4–6 show sample snapshots of the streamwise velocity fluctuations from the D1 database, filtered to retain only the lower axial and azimuthal wave numbers (N_α and N_m), as indicated in Table II, and corresponding estimates obtained using D2, L1, L3, L4, and L5 forcing statistics. Results are shown at radial distances from the pipe wall of $y^+ = (1 - r^+) \approx 15$ and 100 and 200, respectively. In the figures, we use a pseudospanwise coordinate $z = r\theta$ ($\lambda_z = r\lambda_\theta$) to enable comparisons with structures found in planar wall-bounded flows, in particular with the turbulent channel results of our previous work [25]. The white-noise forcing statistics model (white forcing) and the linear operator containing an eddy-viscosity model (EV forcing; see Appendix A) are also considered in the figure as a means of comparison, since with these two models there is no need for prior evaluation of the forcing statistics, considered as white noise.

When considering the buffer layer, at a wall-normal distance of $y^+ \approx 15$, the resemblance between DNS results and the estimates is remarkable, even when the white, eddy-viscosity, and L5 forcing are employed. This is somehow expected, as in the channel flow analysis in [25] we
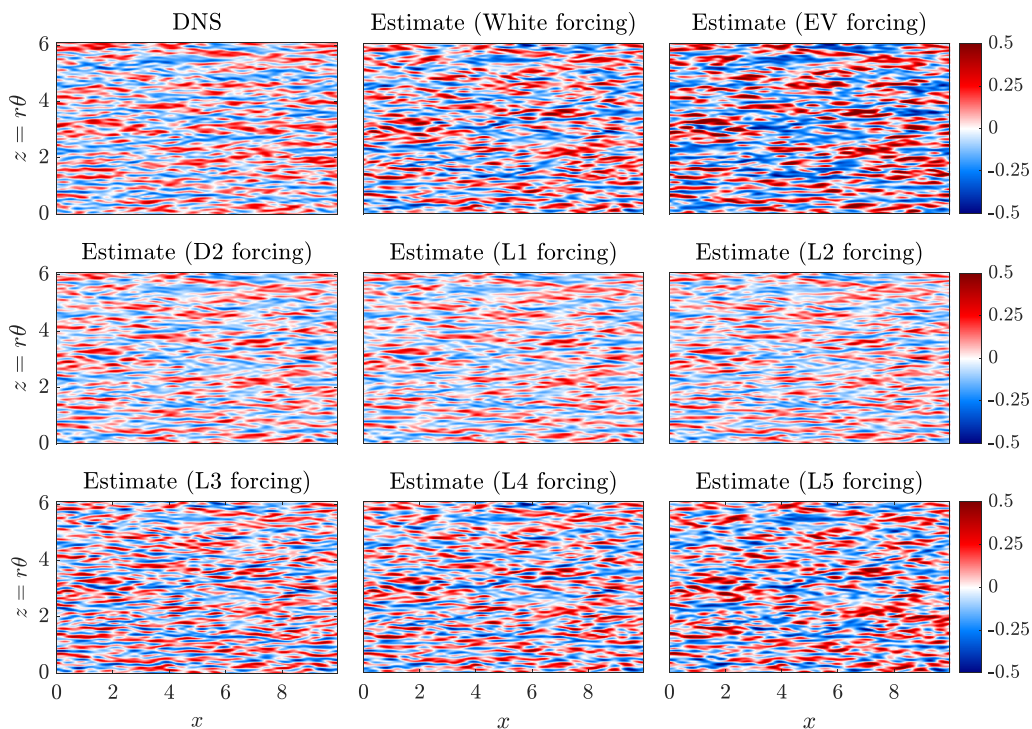
FIG. 4. Comparison between streamwise velocity component instantaneous snapshot of the D1 database and resolvent-based estimates using wall measurements of shear stress and considering white, eddy-viscosity (EV), D2, L1, L3, L4, and L5 forcing statistics at $y^+ \approx 15$. Fluctuations shown in outer units.
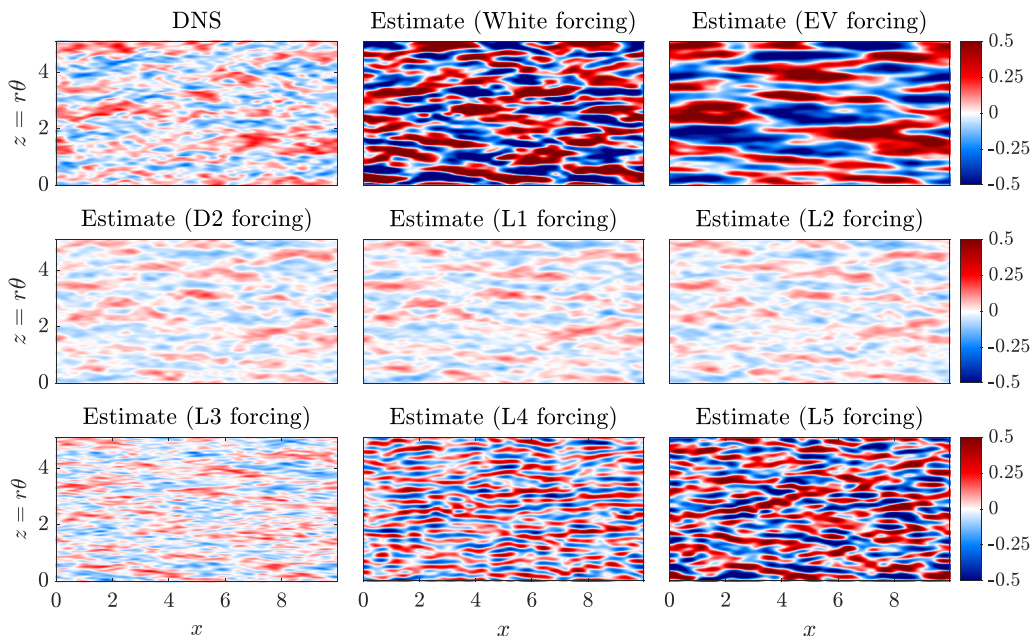

FIG. 5. Comparison between streamwise velocity component instantaneous snapshot of filtered DNS and resolvent-based estimates at $y^+ \approx 100$. See comments in the caption of Fig. 4.
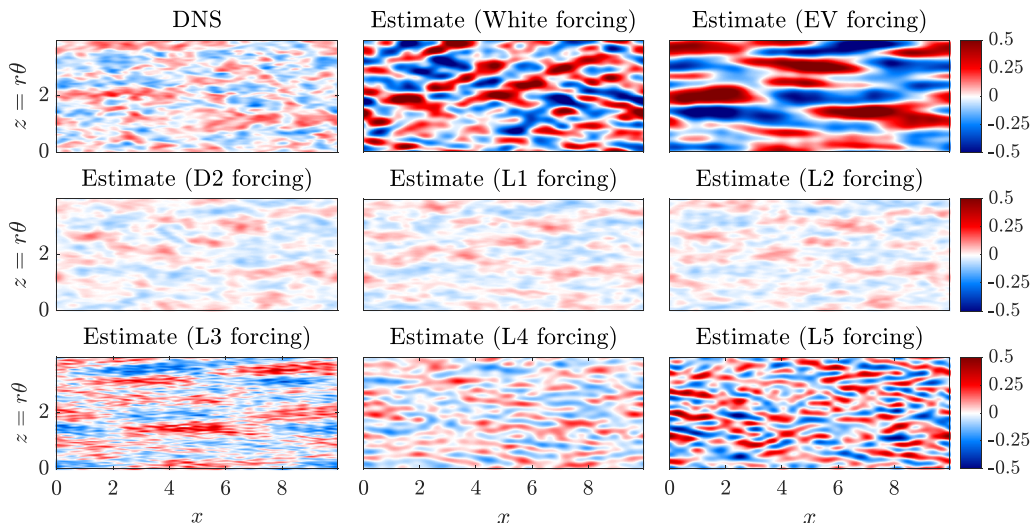
FIG. 6. Comparison between streamwise velocity component instantaneous snapshot of filtered DNS and resolvent-based estimates at $y^+ \approx 200$. See comments in the caption of Fig. 4.

have shown that assuming the forcing statistics to be spatial white noise to build the estimator also provides accurate estimates for distances close to the wall. Regarding quantitative results, as will be seen in the next section, the typical normalized error and correlation at $y^+ \approx 15$ and streamwise velocity fluctuation component are approximately 0.5 and 0.85, respectively, for the D2, L1, and L2 estimators. The L3, L4, L5, spatial white noise, and eddy-viscosity estimators have normalized error of approximately 0.75, 0.8, 1, 0.8, and 1.05, respectively, whereas the correlations are approximately 0.75, 0.7, 0.65, 0.7, and 0.65, respectively. Moving further from the wall, the estimates are not as accurate, especially for the two coarser LES (L4 and L5) estimators, although most of the large-scale structures present in the DNS snapshots are still recognizable in all but the L4 and L5 estimators, as well as the white-noise and eddy-viscosity estimators, in agreement with recent literature [5,29,42]. As one moves further from the wall, only the largest turbulent structures are estimated. For instance, as addressed in Sec. III B, the normalized error and coherence at $y^+ \approx 200$ for the D1, L1, and L2 estimators and streamwise velocity fluctuation component are of approximately 0.9 and 0.4, respectively, whereas the correlations tend to zero and the errors are higher than that for coarser LES.

An interesting observation is that the well-resolved LESs L1 and L2 lead to estimators with similar accuracy to the optimal one, built using the DNS statistics taken from the D2 database. This indicates that LES is a viable approach to obtain forcing statistics to build estimators of wall turbulence, without significant performance degradation if standard grid requirements for wall-resolved LES are used. This may be understood by considering that large-eddy simulations are able to accurately resolve larger turbulent structures, which are the ones that may be estimated from the wall, as seen in earlier studies [7,25,43]. Regarding the radial and azimuthal velocity components, not shown here, similar results to those of the streamwise velocity component were observed.

The small-scale structures can be estimated from the pipe wall even for the coarser LES, white-noise, and eddy-viscosity cases, whereas large-scale structures can be observed up to $y^+ \approx 50$ only for the finer mesh cases. Note that [25] could observe structures up to $y^+ \approx 100$ using the same resolvent-based estimator and only wall-shear stress measurements, but that work built an optimal estimator using the forcing statistics extracted from the reference DNS.
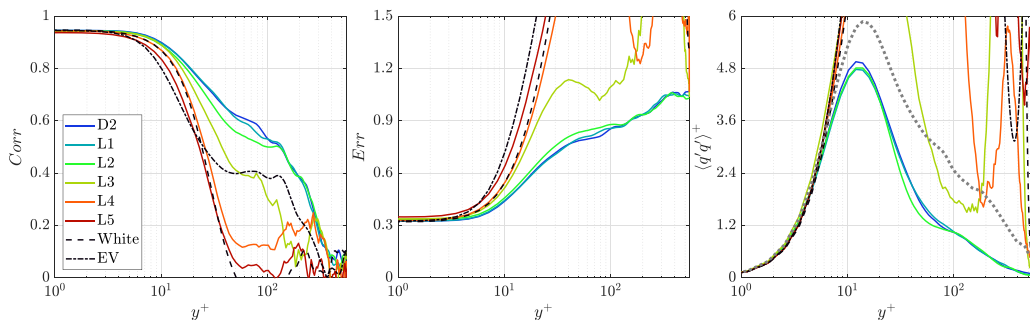
FIG. 7. Flow state comparison metrics for the streamwise velocity fluctuation component. The thick light-gray dotted line in the right frame denotes DNS (D1) variance ($\langle q'q' \rangle^+$) results. Frames, from left to right: correlation, normalized rms, and variance. The DNS variance refers solely to wave numbers retained for estimation.

B. Estimate accuracy

Figure 7 displays normalized correlations (Corr, left frame), rms errors (Err, middle frame), and variance ($\langle q'q' \rangle^+$, right frame) for the streamwise velocity component. Correlation and error metrics are defined, as a function of wall-normal distance y, as

$$\text{Corr}(y) = \frac{\int q_{\text{D1}}(y,t) q_{\text{est}}(y,t) dt}{\sqrt{\int q_{\text{D1}}(y,t)^2 dt} \sqrt{\int q_{\text{est}}(y,t)^2 dt}}, \tag{16a}$$

$$\text{Err}(y) = \frac{\sqrt{\int [q_{\text{est}}(y,t) - q_{\text{D1}}(y,t)]^2 dt}}{\sqrt{\int q_{\text{D1}}(y,t)^2 dt}}, \tag{16b}$$

where q_{D1} denotes a flow state component, e.g., streamwise velocity fluctuation, extracted from the baseline DNS database, and q_{est} denotes an estimated component, from one of the estimators considered here.

Accurate estimates correspond to low normalized error Err, close to 0, and high correlation Corr, close to 1. A sample probe at a given y position was used to evaluate the correlation and error metrics, scanning the complete time series of the baseline (D1) and estimates (D2, L1–L5, white-noise, and eddy-viscosity). The first and last $N_{fft}/2$ instants of the time series were discarded. Such snapshots cannot be estimated due to end effects when computing the convolution using finite time series.

All estimators are accurate up to $y^+ \approx 10$, showing correlation and rms errors of approximately 0.95 and 0.35, respectively, and they were able to correctly identify the streaky structures of the reference DNS. This correlation level very close to the wall is slightly lower than that obtained for $\text{Re}_\tau \approx 550$ turbulent channel flow estimates [25]. However, the channel estimation made use of pressure and wall shear stress from both walls, and forcing terms were directly extracted from the reference DNS, i.e., the same DNS employed for the observations of wall shear-stress and pressure.

Moving farther from the wall, only estimators D2, L1, and L2 maintain the same accuracy, especially regarding the correlation and rms metrics; correlation is higher than 0.5 up to $y^+ \approx 100$. It is interesting that estimator L2, which has a grid with less than 10% of the points used for the DNS-based estimator, could attain such accuracy. This indicates that the large scales are well calculated in the LES, as expected, and their statistics may be used to build an accurate estimator at a fraction of the computational cost of the DNS-based estimator considered in Amaral *et al.* [25].

Figures 8 and 9 show the estimated performance metrics for the radial and azimuthal velocity components, respectively. The plots follow the same trends of the streamwise velocity component
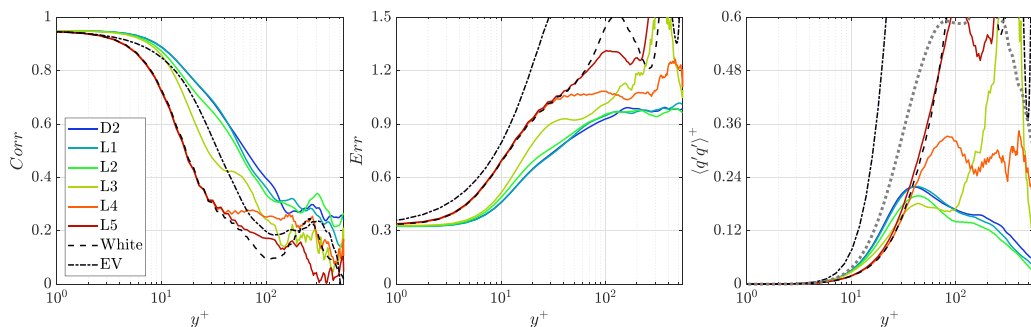
FIG. 8. Flow state comparison metrics for the radial velocity fluctuation component. See comments in the caption of Fig. 7.

metrics, although the effects of loss of coherence, higher error, and mismatch in variance for the two coarser LES grids are more dramatic for the radial and azimuthal velocity components. The estimators built with the finer large-eddy simulations maintain an accuracy similar to that of the DNS estimator based on D2.

To establish a lower-bound case of what is possible to achieve in terms of estimator performance considering cheaper forcing terms modeling, we included a case in which noise forcing statistics are modeled as spatially white (dashed lines in Figs. 7–9) and the linear operator containing an eddy-viscosity model (dash-dotted lines in Figs. 7–9). It is interesting to note that in the near-wall region, up to $y^+ \approx 20$, white noise slightly outperforms the L5 estimator, and the use of the L4 estimator is only justifiable above $y^+ \geqslant 20$. On the other hand, the eddy-viscosity estimator outperforms even the L4 estimator for $y^+ \geqslant 55$, corroborating previous studies [25] that showed the eddy-viscosity model is a good option to model the nonlinear terms of the Navier-Stokes system for distances far from the wall. Overall, the quantitative metrics in Figs. 7–9 confirm the qualitative results shown in Figs. 4–6, although for the azimuthal and radial velocity components the eddy-viscosity model can even outperform the L4 estimator, but not the better resolved LES estimators.

Normalized rms error as a function of the wave-number pair (α, m) and wall-distance y is shown in Fig. 10 for wall distances of $y^+ \approx 15$ and 100. The error metric is defined as

$$\text{Err}(\alpha, y, m) = \frac{\sqrt{\int \sum_{i=1}^{3} \left| q_{\text{est}}^i(\alpha, y, m, t) - q_{\text{D1}}^i(\alpha, y, m, t) \right|^2 dt}}{\sqrt{\int \sum_{i=1}^{3} \left| q_{\text{D1}}^i(\alpha, y, m, t) \right|^2 dt}}, \tag{17}$$
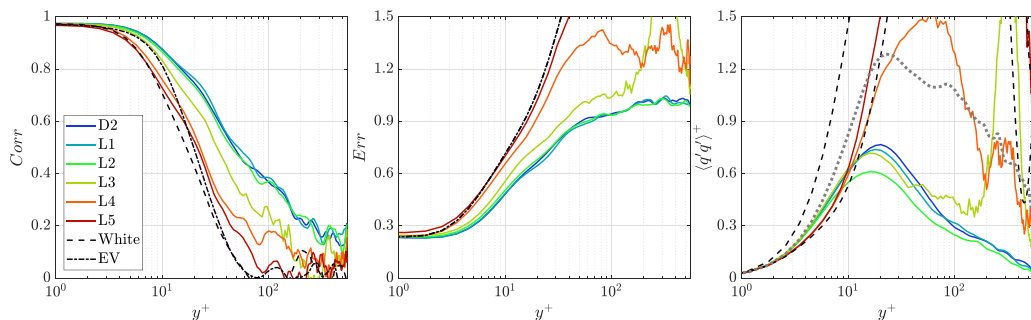

FIG. 9. Flow state comparison metrics for the azimuthal velocity fluctuation component. See comments in the caption of Fig. 7.
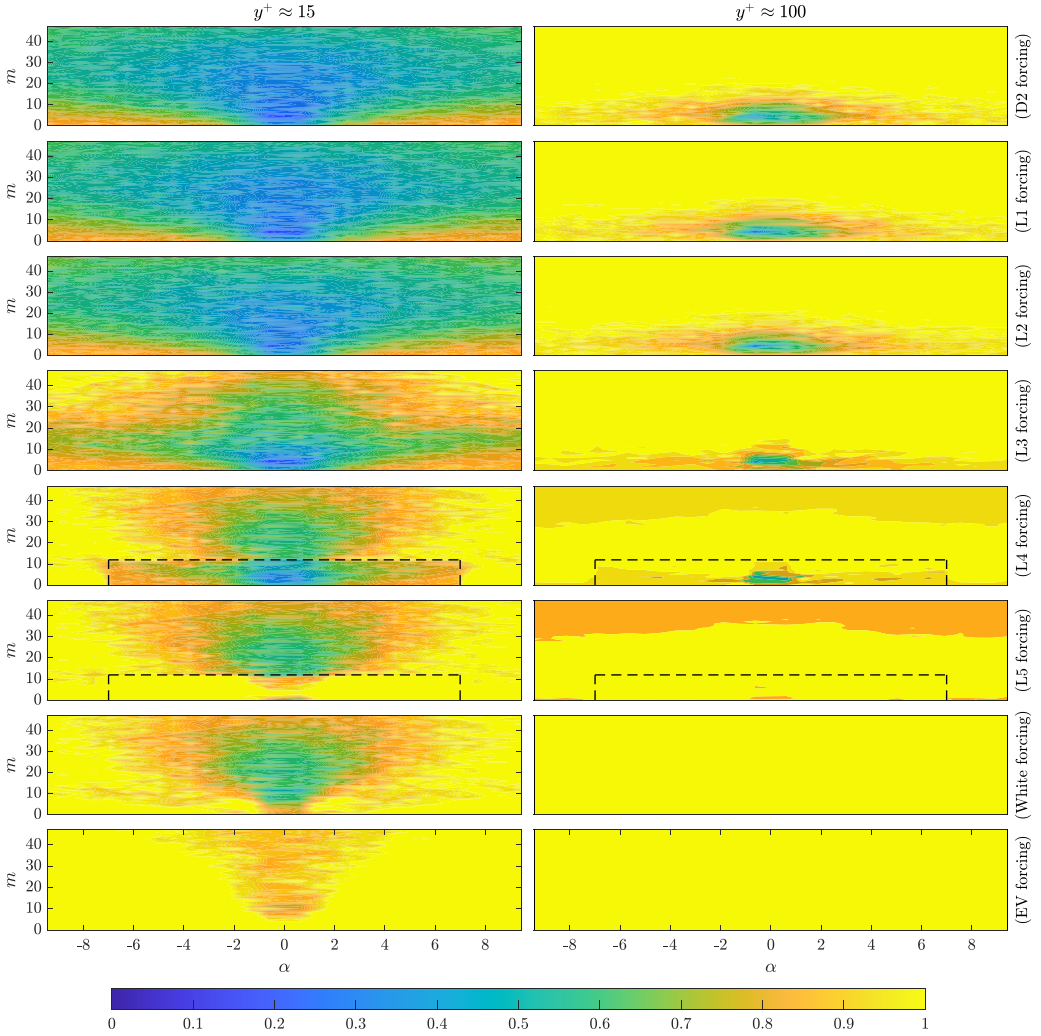
FIG. 10. Normalized rms error as a function of (α, m) state comparison metrics for D2, L1, L2, L3, L4, L5, white-noise, and eddy-viscosity estimators. Normalized errors higher than 1 are saturated.

with superscript i in q^i, for $i = 1$, 2, and 3, denoting streamwise (u_x'), wall-normal/radial (u_r'), and azimuthal (u_θ') velocity fluctuation components, respectively. In this figure, the normalized rms errors are shown in the 0–1 range, and errors higher than 1 are saturated.

Note that for cases L4 and L5 (rows 5 and 6 of Fig. 10), the region delimited by the dashed lines is the region on which the streamwise and azimuthal wave numbers are contained within the LES databases. For the streamwise and azimuthal wave numbers outside that region, the white noise estimator is considered in the calculations, as can be observed on row 8 of Fig. 10.

The large structures, which are characterized by small α and m, are accurately estimated for the D2, L1, and L2 cases, with virtually zero rms error at both planes. The estimates for smaller structures (large α and m), on the other hand, display higher rms error, especially for the $y^+ \approx 100$ plane. For the coarser L4 and L5 estimators, even for the $y^+ \approx 15$ plane, the accuracy of smaller structure estimates is quite low. This indicates that such very coarse LESs are not suitable to build estimators; notice that the grid spacing of L5, of about 100 wall units in the azimuthal direction, is close to the typical streak spacing; hence, near-wall structures cannot be captured by the coarser

LES, which compromises their potential to build resolvent-based estimators. However, the finer LESs allow an accuracy close to that from the optimal D2 estimator, showing that LES is a viable approach to obtain forcing statistics required for resolvent-based estimation. This is far superior to the estimates built from white-noise assumption, also shown in Fig. 10, which have a large error as one moves away from the wall. Inclusion of an eddy viscosity in the operator, also shown in Fig. 10, and consideration of white-noise forcing also leads to inaccurate estimates. This finding is in agreement with recent literature [36] that showed the use of eddy-viscosity models may lead to errors regarding the modeling of turbulent structures.

Regarding the LES requirements to obtain reasonable accurate results, it is observed that simulations with mesh discretization of approximately $\Delta x^+ \leqslant 20$ and $\Delta z^+ \leqslant 12$ provided the best estimates, which agrees with the standards for wall-resolved simulations [7,44]. In other words, we verify here that it is necessary to have a well-resolved LES near the walls to obtain good estimates from measurements obtained at the walls. Our estimates up to the L2 case have error magnitudes that are overall lower than the results presented by Illingworth *et al.* [5] and Oehler *et al.* [12], which employed an eddy-viscosity model and a Kalman filter to estimate turbulent channel flows at $\mathrm{Re}_\tau = 1000$ and 2000, respectively, from streamwise and spanwise velocity measurements; this highlights that the use of forcing statistics from wall-resolved LES is a viable approach to build more accurate estimators. The present results are in agreement with our earlier channel results [25], with the caveat that we are dealing with turbulent pipe flow instead of the channels studied in the cited works.

C. Structures observable from the pipe wall

Smits *et al.* [45] and Jiménez [46], among other authors, have shown that, for wall-bounded flows, many structures leave their footprint on the walls, even the ones present in the outer layer. To explore which flow structures leave a footprint on the walls, in Amaral *et al.* [25] we introduced a metric that consists of a distance from the wall, the maximum observed height, $y_{\mathrm{obs}} = (1 - r_{\mathrm{obs}})$, from which the estimate normalized error is $\mathrm{Err}(\alpha, y_{\mathrm{obs}}, m) \leqslant 0.5$. We select an error value of 0.5, considering that an estimator that attains 50% accuracy or more is good enough, but this value can be calibrated with a more restrictive criterion if desired. As observed in the previous results, the estimators used in this study based on wall measurements of shear stress lose accuracy far from the wall, and only the largest scales may be estimated from wall measurements.

Figure 11 shows the maximum observed height in plus units (y_{obs}^+) as a function of streamwise and pseudospanwise wavelengths $(\lambda_x^+, \lambda_z^+)$, with $\lambda_z = r\lambda_\theta$. Contour levels of $y^+ = 5, 10, 15, 30,$ and 50 are displayed in the maps. For all estimators, the smaller structures (of small-wavelength pairs) can only be well-estimated very close to the wall, whereas far from the wall only large structures (of large-wavelength pairs) can attain some level of accuracy. Estimators D2, L1, L2, and L3 display similar behavior, keeping accuracy for large structures up to $y^+ \approx 50$.

The worse performance of estimators L4 and L5 is mostly associated with smaller structures, which cannot be accurately resolved by the coarser grids. It is interesting to notice that for larger structures, $(\lambda_x^+, \lambda_z^+) \approx (4000, 1000)$, even the coarse-LES estimator L4 maintains some accuracy of estimates, which is in line with the idea that even coarse LESs are able to resolve the largest turbulent structures [47]. However, if the grid is too coarse, there is a worsening of estimates at all scales, as observed from the L5 results, which show a performance lower than the white-noise and eddy-viscosity estimators.

IV. CONCLUSIONS

In this paper, we employed a (linear) resolvent-based estimator methodology [23] to obtain the space-time flow field of a $\mathrm{Re}_\tau \approx 550$ turbulent pipe flow from wall-shear stress low-rank measurements. A DNS database was used to extract the wall-shear stress measurements, whereas other DNS and LES databases were employed for the modeling of the statistics of nonlinear
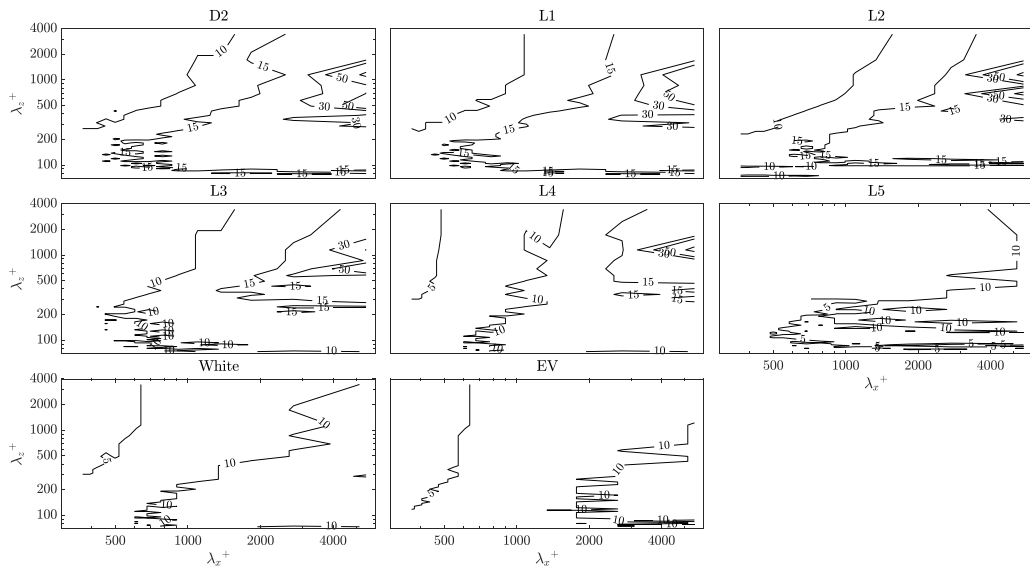
FIG. 11. Observed height in wall/inner units ($y_{obs}^+ = Re_\tau - r_{obs}^+$) for D2, L1, L2, L3, L4, L5, white-noise, and eddy-viscosity estimators.

terms (which constitute a forcing in resolvent analysis) necessary for state estimation. Hence, an optimal estimator, built from DNS statistics, is compared to sub-optimal resolvent-based estimators informed by LES.

We compared the accuracy of the estimators in terms of snapshot reconstruction, correlation, normalized error, and variance. Satisfactory results were obtained with the forcing statistics from LES, especially up to the buffer layer. The accuracy progressively deteriorates for distances far from the wall and for coarser LES meshes, although for cases D2, L1, and L2 the large-scale structures can still be recognizable up to $y^+ \approx 200$. The LES-based estimators using typical grids for wall turbulence maintain an accuracy similar to the optimal estimation built from DNS statistics (D2). The present results are in agreement with recent literature on estimation of wall-bounded flows from wall measurements. For instance, Encinar and Jiménez [7] estimated turbulent structures of channel flows for $932 \leqslant Re_\tau \leqslant 5300$ regimes using a linear stochastic estimator. The authors attained a good level of accuracy near the walls, i.e., at $y/H \approx 0.2$, where H is the channel height. Guastoni *et al.* [9], on the other hand, employed two different convolutional-network algorithms to estimate the instantaneous velocity components of channel flows at $Re_\tau = 180$ and 550, obtaining good agreement with the reference result up to $y^+ = 50$. The question that remains is, at what computational cost can the two above-mentioned strategies attain the same accuracy as the resolvent-based estimator employed together with forcing statistics provided by LES?

The accuracy level of a LES estimator containing approximately 10% of the grid points of the DNS database, case L3 (see Tables I and II), is very close to what is obtained with the DNS estimator, case D2. It would be desirable to be able to estimate flow fluctuations from wall measurements with a simple model for forcing statistics, but the consideration of white-noise forcing leads to inaccurate estimates; hence, a *linear* estimation requires information on the statistics of *nonlinear* terms. The present results show that such statistics of nonlinearity do not need unrealistic levels of accuracy, and moderately coarse large-eddy simulation may provide the required information on dominant nonlinear effects. LES-informed resolvent-based estimation is thus a viable approach for accurate estimates of turbulent flow at high Reynolds numbers, and it can also be seen as a more accurate alternative, with moderate additional cost, to the use of eddy-viscosity models that have been recently explored in the literature for wall-bounded flows [18,27,48,49].

APPENDIX A: EDDY VISCOSITY MODEL

If an eddy-viscosity model is considered, the LNS equations can be written as

$$\partial_t \boldsymbol{u} + u_r \partial_r \bar{U} \boldsymbol{e_x} + \bar{U} \partial_x \boldsymbol{u} = \nabla p + \frac{1}{\text{Re}} \nabla \cdot [\nu_T(r)(\nabla \boldsymbol{u} + \nabla \boldsymbol{u}^T)] + \boldsymbol{f}, \tag{A1a}$$

$$\nabla \cdot \boldsymbol{u} = \boldsymbol{0}, \tag{A1b}$$

where ν_T is the eddy viscosity, which can be modeled as [26]

$$\frac{\nu_T(y)}{\nu} = \frac{1}{2} \left\{ 1 + \frac{\kappa^2 \hat{\text{Re}}^2 \hat{B}}{9} (2y - y^2)^2 (3 - 4y + 2y^2)^2 [1 - e^{(\frac{-y\hat{Re}\sqrt{\hat{B}}}{A^+})}]^2 \right\}^{1/2} + \frac{1}{2}, \tag{A2}$$

where $y = 1 - r$, the constants κ and A^+ are given as 0.42 and 27, respectively [50], $\hat{\text{Re}} = \text{Re}/2$, and $\hat{B} = -2\partial_x p$.

Following Willis *et al.* [51], the linear operator accounting for the eddy-viscosity model is given by

$$A = \begin{bmatrix} -i\alpha\bar{U} + \frac{1}{\text{Re}}[\nu_T(\Delta + r^{-2}) + E] & -D\bar{U} + \frac{1}{\text{Re}}i\alpha\nu_T' & Z & -i\alpha I \\ Z & -i\alpha\bar{U} + \frac{1}{\text{Re}}(\nu_T\Delta + 2E) & -\frac{1}{\text{Re}}F & -D \\ Z & \frac{1}{\text{Re}}(F + i\beta\nu_T'r^{-1}) & -i\alpha\bar{U} + \frac{1}{\text{Re}}(\nu_T\Delta + G) & -i\beta r^{-1} \\ i\alpha I & D + r^{-1} & i\beta r^{-1} & Z \end{bmatrix}, \tag{A3}$$

where

$$\Delta = \nabla^2 - r^{-2} = -\alpha^2 I - (\beta^2 + 1)r^{-2} + r^{-1}D + D^2, \tag{A4a}$$

$$\nu_T' = D\nu_T, \tag{A4b}$$

$$E = \nu_T'D, \tag{A4c}$$

$$F = 2i\beta\nu_T r^{-2}, \tag{A4d}$$

$$G = \nu_T'(D - r^{-1}). \tag{A4e}$$

APPENDIX B: BLOCK SIZE CONVERGENCE TESTS

Figure 12 displays a convergence test for various block sizes ($128 \leqslant N_{fft} \leqslant 2048$) while keeping the block overlap fixed in 75%. The metrics depicted in the figure are the correlation, the normalized error, and the variance of the streamwise velocity fluctuation component. To obtain these results, the forcing terms were extracted from case D2. It is observed that the statistics are well converged in the $256 \leqslant N_{fft} \leqslant 1024$ range. This shows the typical compromise in the application of the Welch method to obtain frequency-domain statistics: blocks that are too short have a low-frequency resolution, while long blocks may lead to worse statistical convergence. It is nonetheless reassuring that various signal-processing choices lead to similar estimation properties. We have taken the
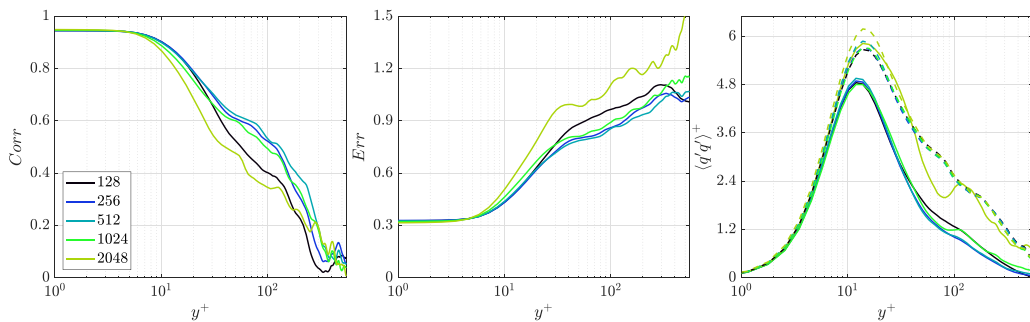
FIG. 12. Flow state comparison metrics for the streamwise velocity fluctuation component and different block sizes using D2 forcing statistics. Dashed curves in the left frame denote DNS (D1) results. Frames, from left to right: correlation, normalized rms, and variance. The DNS variance refers solely to wave numbers retained for estimation.

intermediate value $N_{fft} = 512$ to obtain the forcing statistics used to build the estimators. Similar results, not shown here, were obtained for the radial and azimuthal velocity fluctuation components.

[1] T. R. Bewley and B. Protas, Skin friction and pressure: The "footprints" of turbulence, Physica D **196**, 28 (2004).

[2] J. Hœpffner, M. Chevalier, T. R. Bewley, and D. S. Hennington, State estimation in wall-bounded flow systems. Part 1. Perturbed laminar flows, J. Fluid Mech. **534**, 263 (2005).

[3] M. Chevalier, J. Hœpffner, T. R. Bewley, and D. S. Henningson, State estimation in wall-bounded flow systems. Part 2. Turbulent flows, J. Fluid Mech. **552**, 167 (2006).

[4] C. H. Colburn, J. B. Cessna, and T. R. Bewley, State estimation in wall-bounded flow systems. Part 3. The ensemble Kalman filter, J. Fluid Mech. **682**, 289 (2011).

[5] S. J. Illingworth, J. P. Monty, and I. Marusic, Estimating large-scale structures in wall turbulence using linear models, J. Fluid Mech. **842**, 146 (2018).

[6] Q. Wang, M. Wang, and T. A. Zaki, What is observable from wall data in turbulent channel flow? J. Fluid Mech. **941**, A48 (2022).

[7] M. P. Encinar and J. Jiménez, Logarithmic-layer turbulence: A view from the wall, Phys. Rev. Fluids **4**, 114603 (2019).

[8] K. Sasaki, R. Vinuesa, A. V. G. Cavalieri, P. Schlatter, and D. S. Henningson, Transfer functions for flow predictions in wall-bounded turbulence, J. Fluid Mech. **864**, 708 (2019).

[9] L. Guastoni, A. Güemes, A. Ianiro, S. Discetti, P. Schlatter, H. Azizpour, and R. Vinuesa, Convolutional-network models to predict wall-bounded turbulence from wall quantities, J. Fluid Mech. **928**, A27 (2021).

[10] A. Nekkanti and O. T. Schmidt, Gappy spectral proper orthogonal decomposition, J. Comput. Phys. **478**, 111950 (2023).

[11] B. J. McKeon, The engine behind (wall) turbulence: Perspectives on scale interactions, J. Fluid Mech. **817**, P1 (2017).

[12] S. Oehler, A. Garcia-Gutiérrez, and S. Illingworth, Linear estimation of coherent structures in wall-bounded turbulence at $Re_\tau = 2000$, J. Phys.: Conf. Ser. **1001**, 012006 (2018).

[13] G. Tissot, A. V. G. Cavalieri, and É. Mémin, Stochastic linear modes in a turbulent channel flow, J. Fluid Mech. **912**, A51 (2021).

[14] B. Herrmann, P. J. Baddoo, R. Semaan, S. L. Brunton, and B. J. McKeon, Data-driven resolvent analysis, J. Fluid Mech. **918**, A10 (2021).

[15] B. Lopez-Doriga, S. T. M. Dawson, and R. Vinuesa, Resolvent analysis of laminar and turbulent duct flows, arXiv:2205.13630.

[16] S. Symon, A. Madhusudanan, S. J. Illingworth, and I. Marusic, Use of eddy viscosity in resolvent analysis of turbulent channel flow, Phys. Rev. Fluids **8**, 064601 (2023).

[17] B. J. McKeon and A. S. Sharma, A critical-layer framework for turbulent pipe flow, J. Fluid Mech. **658**, 336 (2010).

[18] Y. Hwang and C. Cossu, Linear non-normal energy amplification of harmonic and stochastic forcing in the turbulent channel flow, J. Fluid Mech. **664**, 51 (2010).

[19] S. Beneddine, D. Sipp, A. Arnault, J. Dandois, and L. Lesshafft, Conditions for validity of mean flow stability analysis, J. Fluid Mech. **798**, 485 (2016).

[20] K. Taira, S. L. Brunton, S. T. M. Dawson, C. W. Rowley, T. Colonius, B. J. McKeon, O. T. Schmidt, S. Gordeyev, V. Theofilis, and L. S. Ukeiley, Modal analysis of fluid flows: An overview, AIAA J. **55**, 4013 (2017).

[21] S. Bagheri, D. S. Henningson, J. Hoepffner, and P. J. Schmid, Input-output analysis and control design applied to a linear model of spatially developing flows, Appl. Mech. Rev. **62**, 020803 (2009).

[22] A. Towne, A. Lozando-Durán, and X. Yang, Resolvent-based estimation of space–time flow statistics, J. Fluid Mech. **883**, A17 (2020).

[23] E. Martini, P. Jordan, A. V. G. Cavalieri, A. Towne, and L. Lesshafft, Resolvent-based optimal estimation of transitional and turbulent flows, J. Fluid Mech. **900**, A2 (2020).

[24] E. Martini, J. Jung, A. V. G. Cavalieri, P. Jordan, and A. Towne, Resolvent-based tools for optimal estimation and control via the wiener-hopf formalism, J. Fluid Mech. **937**, A19 (2022).

[25] F. R. Amaral, A. V. G. Cavalieri, E. Martini, P. Jordan, and A. Towne, Resolvent-based estimation of turbulent channel flow using wall measurements, J. Fluid Mech. **927**, A17 (2021).

[26] R. D. Cess, A survey of the literature on heat transfer in turbulent tube flow, Technical Report No. 8-0529-R24, Westinghouse Research, 1958.

[27] J. C. del Álamo and J. Jiménez, Linear energy amplification in turbulent channels, J. Fluid Mech. **559**, 205 (2006).

[28] V. K. Chinta and M. Luhar, Statistically consistent resolvent-based reconstruction of turbulent channel flows from limited measurements, in *12th International Symposium on Turbulence and Shear Flow Phenomena (TSFP12), Osaka, Japan* (2022), p. 112, http://www.tsfp-conference.org/proceedings/2022/112.pdf.

[29] P. Morra, P. A. S. Nogueira, A. V. G. Cavalieri, and D. S. Henningson, The colour of forcing statistics in resolvent analyses of turbulent channel flows, J. Fluid Mech. **907**, A24 (2021).

[30] M. Luhar, A. S. Sharma, and B. J. McKeon, Opposition control within the resolvent analysis framework, J. Fluid Mech. **749**, 597 (2014).

[31] A. Zare, M. R. Jovanović, and T. T. Georgiou, Colour of turbulence, J. Fluid Mech. **812**, 636 (2017).

[32] U. Karban, E. Martini, A. V. G. Cavalieri, L. Lesshafft, and P. Jordan, Self-similar mechanisms in wall turbulence studied using resolvent analysis, J. Fluid Mech. **939**, A36 (2022).

[33] A. Zare, T. T. Georgiou, and M. R. Jovanović, Stochastic dynamical modeling of turbulent flows, Annu. Rev. Control Robot. Auton. Syst. **3**, 195 (2020).

[34] M. R. Jovanović, From bypass transition to flow control and data-driven turbulence modeling: An input–output viewpoint, Annu. Rev. Fluid Mech. **53**, 311 (2021).

[35] D. B. S. Audiffred, A. V. G. Cavalieri, P. P. C. Brito, and E. Martini, Experimental control of Tollmien-Schlichting waves using the Wiener-Hopf formalism, Phys. Rev. Fluids **8**, 073902 (2023).

[36] S. Symon, S. J. Illingworth, and I. Marusic, Energy transfer in turbulent channel flows and implications for resolvent modelling, J. Fluid Mech. **911**, A3 (2021).

[37] A. P. Willis, The Openpipeflow Navier-Stokes solver, SoftwareX **6**, 124 (2017).

[38] J. Smagorinsky, General circulation experiments with the primitive equations: I. The basic experiment, Mon. Weather Rev. **91**, 99 (1963).

[39] E. R. Van Driest, On turbulent flow near a wall, J. Aeronaut. Sci. **23**, 1007 (1956).

[40] P. D. Welch, The use of Fast Fourier Transform for the estimation of power spectra: A method based on time averaging over short, modified periodograms, IEEE Trans. Audio Electroacoust. **15**, 70 (1967).

[41] G. K. El Khoury, P. Schlatter, A. Noorani, P. F. Fischer, G. Brethouwer, and A. V. Johansson, Direct numerical simulation of turbulent pipe flow at moderately high Reynolds numbers, Flow Turbul. Combust. **91**, 475 (2013).

[42] L. I. Abreu, A. V. G. Cavalieri, P. Schlatter, R. Vinuesa, and D. S. Henningson, Resolvent modelling of near-wall coherent structures in turbulent channel flow, Int. J. Heat Fluid Flow **85**, 108662 (2020).

[43] M. Wang and T. A. Zaki, State estimation in turbulent channel flow from limited observations, J. Fluid Mech. **917**, A9 (2021).

[44] A. Rasam, G. Brethouwer, P. Schlatter, Q. Li, and A. V. Johansson, Effects of modelling, resolution and anisotropy of subgrid-scales on large eddy simulations of channel flow, J. Turbul. **12**, N10 (2011).

[45] A. J. Smits, B. J. McKeon, and I. Marusic, High-Reynolds number wall turbulence, Annu. Rev. Fluid Mech. **43**, 353 (2011).

[46] J. Jiménez, Near-wall turbulence, Phys. Fluids **25**, 101302 (2013).

[47] A. Rasam, S. Wallin, G. Brethouwer, and A. V. Johansson, Improving separated-flow predictions using an anisotropy-capturing subgrid-scale model, Int. J. Heat Fluid Flow **65**, 246 (2017).

[48] P. Morra, O. Semeraro, D. S. Henningson, and C. Cossu, On the relevance of Reynolds stresses in resolvent analyses of turbulent wall-bounded flows, J. Fluid Mech. **867**, 969 (2019).

[49] E. Pickering, G. Rigas, O. T. Schmidt, D. Sipp, and T. Colonius, Optimal eddy viscosity for resolvent-based models of coherent structures in turbulent jets, J. Fluid Mech. **917**, A29 (2021).

[50] B. J. McKeon, M. V. Zagarola, and A. J. Smits, A new friction factor relationship for fully developed pipe flow, J. Fluid Mech. **538**, 429 (2005).

[51] A. P. Willis, Y. Hwang, and C. Cossu, Optimally amplified large-scale streaks and drag reduction in turbulent pipe flow, Phys. Rev. E **82**, 036321 (2010).